



Efficient spatiotemporal-vortex four-wave mixing in a semiconductor nanostructureZhiping Wang ^{1,2,*}, Yufeng Zhang,^{1,2} Emmanuel Paspalakis ^{3,†} and Benli Yu^{1,2}¹*Information Materials and Intelligent Sensing Laboratory of Anhui Province, Anhui University, Hefei 230601, China*²*Key Laboratory of Opto-Electronic Information Acquisition and Manipulation, Ministry of Education, Anhui University, Hefei 230601, China*³*Materials Science Department, School of Natural Sciences, University of Patras, Patras 265 04, Greece*

(Received 28 July 2020; accepted 16 November 2020; published 7 December 2020)

We propose a scheme to demonstrate spatiotemporal-vortex four-wave mixing (FWM) in an asymmetric semiconductor double quantum-well nanostructure. It is found that the orbital-angular-momentum (OAM) phase is transferred entirely from a unique OAM mode to the FWM field. Interestingly, by adjusting the detuning or the intensity of a control field, one can effectively modulate the phase and intensity of the FWM field. Also, we perform the superposition modes created by the interference between the FWM field and a same-frequency Laguerre-Gaussian mode, which show many interesting properties. Moreover, the conversion efficiency and quality of the output FWM field are studied. It is shown that the generated FWM mode has a maximum fidelity of approximately 100%. Our result may find potential applications in fundamental research and quantum technologies based on OAM light in solids.

DOI: [10.1103/PhysRevA.102.063509](https://doi.org/10.1103/PhysRevA.102.063509)**I. INTRODUCTION**

A vortex beam carrying orbital angular momentum (OAM), unlike a conventional Gaussian beam, is characterized by a helical wave front and has a more complex spatial distribution [1,2]. Based on OAM beams, much progress has been made in the interaction between vortex beams and atomic media. For example, four-wave mixing (FWM) with OAM has been experimentally investigated in atomic media [3–6]. The transfer of OAM between light beams based on FWM has been reported in atomic vapors [7–9] and has been explored theoretically in several works [10–14]. The storage and memory of OAM have been demonstrated in atomic gases [15–17]. Quite recently, entanglement via spatial FWM processes in hot atoms has also been presented [18,19].

On the other hand, there has been an increasing interest in quantum phenomena in semiconductor quantum wells (SQWs). It has been shown that electromagnetically induced transparency (EIT) [20–22], coherent population trapping [23], all-optical switching [24], lasing without inversion [25], Kerr nonlinearity [26], optical bistability [27], optical solitons [28,29], and four-wave mixing [30–33] are possible in such solid-state systems. However, these studies do not take into account the spatial characteristics of the optical fields.

In this paper, we investigate the spatiotemporal-vortex FWM in an asymmetric semiconductor double quantum-well (SDQW) nanostructure on the condition of low temperatures up to 10 K. Recently, we have proposed two schemes to control vortex FWM with OAM via single-photon detuning [34] or two-photon resonance [35] in SQWs. In addition, spatially structured transparency [36] and the transfer of

optical vortices via three-wave mixing [37] in quantum-dot nanostructures have also been proposed. However, different from these previous studies, the distinguishing features of this scheme are given as follows: First and foremost, the FWM field transferred from a unique OAM mode, which is shaped as a double-ring Laguerre-Gaussian (LG) beam with a radial index $p = 1$ and an azimuthal index l , is equal but opposite in the inner ring and the outer ring. Second, by adjusting the detuning Δ_c or the intensity of the control field Ω_c , the phase and intensity of the FWM field can be drastically manipulated. In particular, by an appropriate choice of the intensity of the control field Ω_c , the FWM field can be significantly enhanced and the phase twist is almost completely suppressed. This is a significant advantage of our proposed scheme compared with Ref. [34]. Third, we show the superposition modes created by the interference between the FWM field and a same-frequency LG beam, which show a more flexible intensity control or phase control for superposition OAM modes. Furthermore, different from the previous scheme [34], we consider the conversion efficiency and fidelity of the output FWM field here. It is found that the FWM conversion efficiency is more than 20% and the generated FWM mode has a fidelity approximately 100% in comparison to the input OAM mode. Compared with the FWM processes in atomic gases [38–41], the solid-state materials [42–44] are much more practical than the atomic counterparts. Thus, the modulation in such a solid-state system could be useful for manipulating the OAM beams [45–48].

II. MODEL AND GOVERNING EQUATIONS

As it is shown in Fig. 1, we consider a SDQW nanostructure consisting of 50 modulation-doped SDQWs, which is assumed to be grown on a GaAs substrate. Each period consists of two GaAs wells, respectively, 70 and 60 Å thick,

*Corresponding author: wzping@mail.ustc.edu.cn†paspalak@upatras.gr

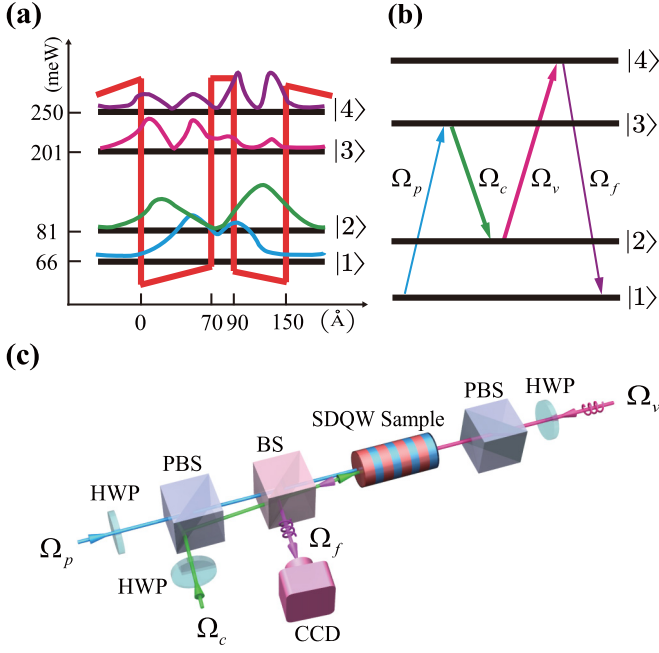


FIG. 1. (a) Schematic energy-band diagram of a single period of the asymmetric SDQW nanostructure. (b) The energy-level arrangement. (c) A simple diagram of the FWM setup. The probe field Ω_p and the control field Ω_c are focused inside the sample. Their diameters are $3\omega_0$. The OAM field Ω_v is collimated and has a waist ω_0 . The three of them are made to be coincided inside the sample, and the FWM field Ω_f is generated under the phase-matching condition. The FWM field is collected by a CCD camera. HWP: half-wave plate; PBS: polarization beam splitter; BS: beam splitter; CCD: charge-coupled device.

separated by a 20-Å $\text{Al}_{0.33}\text{Ga}_{0.67}\text{As}$ barrier. The coupled-well periods are separated by a 950-Å $\text{Al}_{0.33}\text{Ga}_{0.67}\text{As}$ spacer layer. The SDQW sample considered here is similar to the one reported in Ref. [49] and we can choose the proper parametric conditions. The sample can be designed to have the desired transition energies, i.e., $E_{13} = 136.2$ meV, $E_{14} = 184.4$ meV, $E_{23} = 120$ meV, and $E_{24} = 168$ meV. The energy levels and wave functions [see Fig. 1(a)] are calculated by solving self-consistently the Schrödinger and Poisson's equation in the envelope-function formalism [50]. This system interacts with a probe field $\Omega_p = \Omega_{p0} \exp[(x^2 + y^2)^8 / \omega_{p0}^{16}] \exp(-t^2 / \tau^2)$ (ω_{p0} and Ω_{p0} are the transverse waist and initial amplitude with τ being the pulse length), a continuous-wave (cw) control field Ω_c , and a OAM field Ω_v , then a FWM field Ω_f can be generated efficiently [see Fig. 1(c)]. Note that the OAM field Ω_v is a LG mode [51], which takes the form

$$\Omega_v = \begin{cases} \Omega_{v0} \Omega(r) e^{-i\phi l}, & \text{inner ring,} \\ \Omega_{v0} \Omega(r) e^{i\phi l}, & \text{outer ring,} \end{cases} \quad (1)$$

where $\Omega(r) = \frac{\sqrt{2p!/\pi(p+|l|)!}}{\omega_0} \left(\frac{\sqrt{2}r}{\omega_0}\right)^{|l|} L_p^{|l|} \left(\frac{2r^2}{\omega_0^2}\right) e^{-r^2/\omega_0^2}$, Ω_{v0} is the amplitude, r is the radius, $L_p^{|l|}$ is the Laguerre polynomial, ϕ is the azimuthal angle, and ω_0 is the waist size of the LG mode. Also, l and p describe the azimuthal index and radial index. In this work, we keep the radial index $p = 1$ while the azimuthal index l is equal but opposite in the inner ring [$0 \leq r \leq$

$\sqrt{0.5(|l| + 1)}\omega_0$] and the outer ring [$r \geq \sqrt{0.5(|l| + 1)}\omega_0$]. Additionally, we disregard the propagation effect of the LG mode; indeed, interesting aspects [52,53] may appear if this effect is considered.

In the following analysis, we have neglected other many-body effects such as the depolarization effect, which renormalizes the free-carrier and carrier-field contributions. Also, the SDQWs are designed with low dopings such that electron-electron effects have very small influences on our results [54]. Under the rotating-wave approximation and electric-dipole approximation, the Hamiltonian is given as ($\hbar = 1$)

$$H = \Delta_c |2\rangle\langle 2| + \Delta_p |3\rangle\langle 3| + \Delta_v |4\rangle\langle 4| - (\Omega_p e^{i\mathbf{k}_p \cdot \mathbf{r}} |3\rangle\langle 1| + \Omega_c e^{i\mathbf{k}_c \cdot \mathbf{r}} |3\rangle\langle 2| + \Omega_v e^{i\mathbf{k}_v \cdot \mathbf{r}} |4\rangle\langle 2| + \Omega_f e^{i\mathbf{k}_f \cdot \mathbf{r}} |4\rangle\langle 1| + \text{H.c.}), \quad (2)$$

where the detunings are defined as $\Delta_c = \epsilon_{21} - (\omega_p - \omega_c)$, $\Delta_p = \epsilon_{31} - \omega_p$, and $\Delta_v = \epsilon_{41} - (\omega_p - \omega_c + \omega_v)$, respectively. ϵ_{21} , ϵ_{31} , and ϵ_{41} are the energy differences of the $|2\rangle \leftrightarrow |1\rangle$, $|3\rangle \leftrightarrow |1\rangle$, and $|4\rangle \leftrightarrow |1\rangle$ intersubband transitions. Also, ω_c , ω_v , and ω_p are the central frequencies of three fields. By adjusting the frequencies of the fields, one can effectively modulate the detunings. \mathbf{r} is the position vector. The wave vectors of the relevant field are defined as \mathbf{k}_j ($j = p, c, v, f$).

Defining the electronic energy state as $|\psi\rangle = (A_1, A_2 e^{i(\mathbf{k}_p - \mathbf{k}_c) \cdot \mathbf{r}}, A_3 e^{i\mathbf{k}_p \cdot \mathbf{r}}, A_4 e^{i(\mathbf{k}_p - \mathbf{k}_c + \mathbf{k}_v) \cdot \mathbf{r}})^T$ (T is a transpose) and using the Schrödinger equation $i\partial_t |\psi\rangle = H |\psi\rangle$, the equations for the probability amplitudes A_j ($j = 1 - 4$) of the electronic wave functions are written as

$$\dot{A}_1 = i\Omega_p^* A_3 + i\Omega_f^* A_4 e^{i\delta \mathbf{k} \cdot \mathbf{r}}, \quad (3a)$$

$$\dot{A}_2 = -(i\Delta_c + \gamma_2) A_2 + i\Omega_v^* A_4 + i\Omega_c^* A_3, \quad (3b)$$

$$\dot{A}_3 = -(i\Delta_p + \gamma_3) A_3 + i\Omega_c A_2 + i\Omega_p A_1, \quad (3c)$$

$$\dot{A}_4 = -(i\Delta_v + \gamma_4) A_4 + i\Omega_f A_1 e^{-i\delta \mathbf{k} \cdot \mathbf{r}} + i\Omega_v A_2, \quad (3d)$$

where $\delta \mathbf{k} = \mathbf{k}_p + \mathbf{k}_v - \mathbf{k}_c - \mathbf{k}_f$. The $\gamma_{2,3,4}$ are added phenomenologically [20] to describe the overall decay rates of the subbands $|2\rangle$, $|3\rangle$, and $|4\rangle$.

Under the slowly varying amplitude approximation, the following Maxwell equations describe the propagations of the probe and FWM fields,

$$\frac{\partial \Omega_p}{\partial z} + \frac{\partial \Omega_p}{\partial t} = \frac{ic}{2\omega_p} \nabla_{\perp}^2 \Omega_p + ik_p A_3 A_1^*, \quad (4a)$$

$$\frac{\partial \Omega_f}{\partial z} + \frac{\partial \Omega_f}{\partial t} = \frac{ic}{2\omega_f} \nabla_{\perp}^2 \Omega_f + ik_f A_4 A_1^*, \quad (4b)$$

where $k_p = 2\pi N \omega_p |\mu_{31}|^2 / (c\hbar)$ and $k_f = 2\pi N \omega_f |\mu_{41}|^2 / (c\hbar)$ are two propagation constants, which are related to the frequently used oscillator strengths of the subband transitions $|3\rangle \leftrightarrow |1\rangle$ and $|4\rangle \leftrightarrow |1\rangle$. Here, $\mu_{31(41)}$ are the dipole moments of the respective transitions and N is the electron density. The first terms on the right-hand sides of Eqs. (7) and (8) account for light diffraction, which can be neglected if the propagation distance is much smaller than the Rayleigh ranges of the probe field or the FWM field, i.e., $\pi \omega_{p(f)}^2 / \lambda_{p(f)} \gg L$. Here, we consider the propagation distance $L = 200 \mu\text{m}$, the waist $\omega_{p(f)} \approx 600 \mu\text{m}$ ($200 \mu\text{m}$), and the wavelength $\lambda_{p(f)} \approx 9.2 \mu\text{m}$ ($6.7 \mu\text{m}$) [49], obtaining $\pi \omega_{p(f)}^2 / \lambda_{p(f)} \approx$

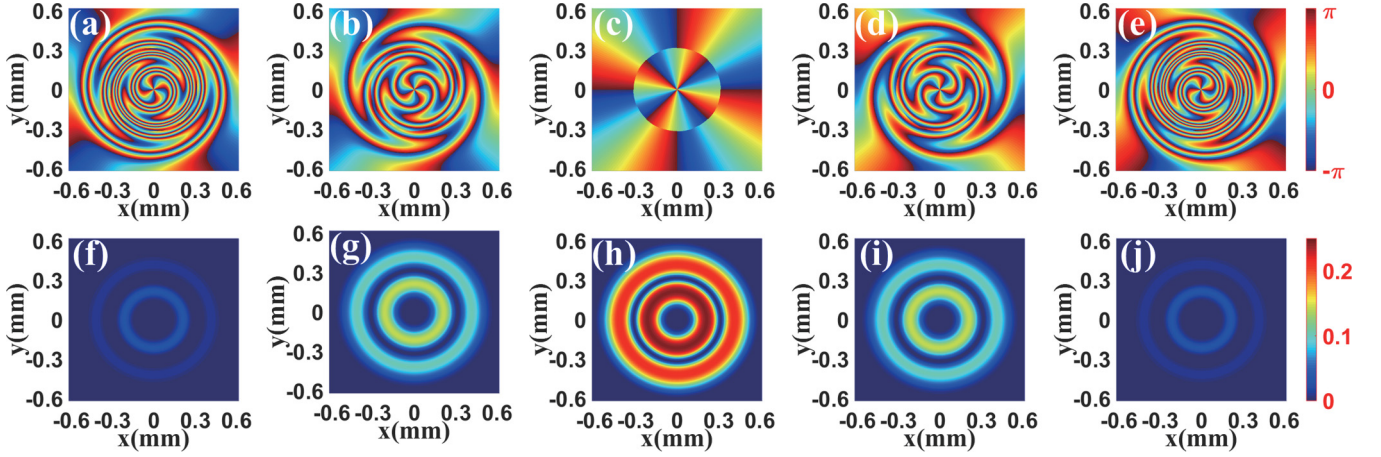


FIG. 2. The phase [(a)–(e)] and intensity [(f)–(j)] profiles of the FWM field for different detunings Δ_c : (a) and (f) $\Delta_c = -20$ meV, (b) and (g) $\Delta_c = -10$ meV, (c) and (h) $\Delta_c = 0$ meV, (d) and (i) $\Delta_c = 10$ meV, (e) and (j) $\Delta_c = 20$ meV. Other parameters are $\Delta_p = \Delta_v = 0$, $l = 4$, $\Omega_{p0} = 1$ meV, $\Omega_c = 20$ meV, $\Omega_{v0} = 15$ meV, $\gamma_2 = 2.36 \times 10^{-6}$ meV, $\gamma_3 = 1.32$ meV, $\gamma_4 = 1.3$ meV, $\omega_0 = 0.2$ mm, $\omega_{p0} = 3\omega_0$, $L = 200 \mu\text{m}$, $k_p = k_f = 9.6$ meV/ μm and $\tau = 10^{-6}$ s.

$1.228 \times 10^5 \mu\text{m}$ ($1.87 \times 10^4 \mu\text{m}$) $\gg 200 \mu\text{m}$. So we ignore the diffraction terms safely.

Since the probe field is weak, most electrons remain in the subband level $|1\rangle$, so we assume $|A_1|^2 \approx 1$. Then, the Fourier transformation of the related Maxwell-Bloch Eqs. (3) and (4) under the phase-matching condition $\delta\mathbf{k} = \mathbf{0}$ is given by

$$M_2 a_2 + \Omega_c^* a_3 + \Omega_v^* a_4 = 0, \quad (5a)$$

$$M_3 a_3 + \Omega_c a_2 = -W_p, \quad (5b)$$

$$M_4 a_4 + \Omega_v a_2 = -W_f, \quad (5c)$$

$$\frac{\partial W_p}{\partial z} - i\omega \frac{W_p}{c} = ik_p a_3 a_1^*, \quad (5d)$$

$$\frac{\partial W_f}{\partial z} - i\omega \frac{W_f}{c} = ik_f a_4 a_1^*, \quad (5e)$$

where $M_2 = \omega - \Delta_c + i\gamma_2$, $M_3 = \omega - \Delta_p + i\gamma_3$, $M_4 = \omega - \Delta_v + i\gamma_4$, a_j ($j = 1, 2, 3, 4$), and $W_{p(f)}$ are the Fourier transforms of A_j and $\Omega_{p(f)}$, respectively. Based on Eqs. (9)–(11), we obtain

$$a_3 = (\Omega_c \Omega_v^* W_f + D_p W_p) / D, \quad (6a)$$

$$a_4 = (\Omega_c^* \Omega_v W_p + D_f W_f) / D, \quad (6b)$$

with $D_p = M_2 M_4 - |\Omega_v|^2$, $D_f = M_2 M_3 - |\Omega_c|^2$, and $D = M_4 |\Omega_c|^2 + M_3 |\Omega_v|^2 - M_2 M_3 M_4$.

Using the initial conditions for the probe and FWM field, i.e., $W_p(z = 0, \omega) \neq 0$ and $W_f(z = 0, \omega) = 0$, the analytic solution for the FWM field is

$$W_f(z, \omega) = \frac{k_f \Omega_c^* \Omega_v W_p(0, \omega)}{\sqrt{G}} (e^{izK_+} - e^{izK_-}), \quad (7)$$

where $K_{\pm} = \omega/c + (k_p D_p + k_f D_f \pm \sqrt{G}) / 2D = K_{\pm}^{(0)} + K_{\pm}^{(1)} + O(\omega^2)$, with $G = (k_p D_p - k_f D_f)^2 + 4|\Omega_c|^2 |\Omega_v|^2 k_f k_p$.

In Eq. (7), one readily sees that there exist two modes described by the dispersion relations K_+ and K_- , respectively. Based on Ref. [55], the K_- mode is absorbed quickly and only the K_+ mode remains after a short propagation distance L at

the central frequency. By neglecting the K_- mode and using the inverse Fourier transform for $W_f(z, \omega)$, we arrive at the FWM field,

$$\Omega_f(L, t) = \begin{cases} \tilde{\Omega}_f e^{-i\phi l} e^{iLK_+}, & \text{inner ring,} \\ \tilde{\Omega}_f e^{i\phi l} e^{iLK_+}, & \text{outer ring,} \end{cases} \quad (8)$$

where $\tilde{\Omega}_f = k_f \Omega_c^* \Omega_v \Omega(r) \Omega_p(0, t - L/V_g) / \sqrt{G}$, and $V_g = 1/\text{Re}[K_+^{(1)}]$ is the group velocity. From Eq. (8), one can find the FWM field $\Omega_f(L, t) \sim e^{\pm i l \phi}$ is generated with the same vorticity as the OAM field $\Omega_v \sim e^{\pm i l \phi}$, which implies the OAM phase of field Ω_v is entirely transferred to the FWM field.

Normally, the real part $\text{Re}(K_+)$ represents the variation of the phase per unit length while the imaginary part $\text{Im}(K_+)$ represents the absorption [56]. Using $K_+ = \text{Re}(K_+) + i \text{Im}(K_+)$ we can rewrite Eq. (8) as

$$\Omega_f(L, t) = \begin{cases} \tilde{\Omega}_f e^{-L \text{Im}(K_+)} e^{-i[\phi l - L \text{Re}(K_+)]}, & \text{inner ring,} \\ \tilde{\Omega}_f e^{-L \text{Im}(K_+)} e^{i[\phi l + L \text{Re}(K_+)]}, & \text{outer ring,} \end{cases} \quad (9)$$

where we can see the intensity of the FWM field is $\propto |\tilde{\Omega}_f e^{-L \text{Im}(K_+)}|^2$. The factor $e^{-i[\phi l - L \text{Re}(K_+)]}$ reflects the phase of the FWM field in the inner ring, while the factor $e^{i[\phi l + L \text{Re}(K_+)]}$ reflects the phase of the FWM field in the outer ring. Obviously, both the phase and intensity of the FWM field can be modulated via the dispersion-relation term K_+ .

III. RESULTS

A. Manipulation of four-wave mixing

Figure 2 shows the phase and intensity profiles of the FWM field for different detunings Δ_c . When the detuning Δ_c is tuned to 0, the phase is normal and the intensity displays a double-ring pattern [see Figs. 2(c) and 2(h)]. As we adjust the detuning Δ_c to -10 meV and then to -20 meV, the phase twist becomes more and more serious and the intensity becomes more and more weak [see Figs. 2(a), 2(b), 2(f), and 2(g)], and the phases within the inner ring ($0 \leq r \leq \sqrt{2.5}\omega_0$)

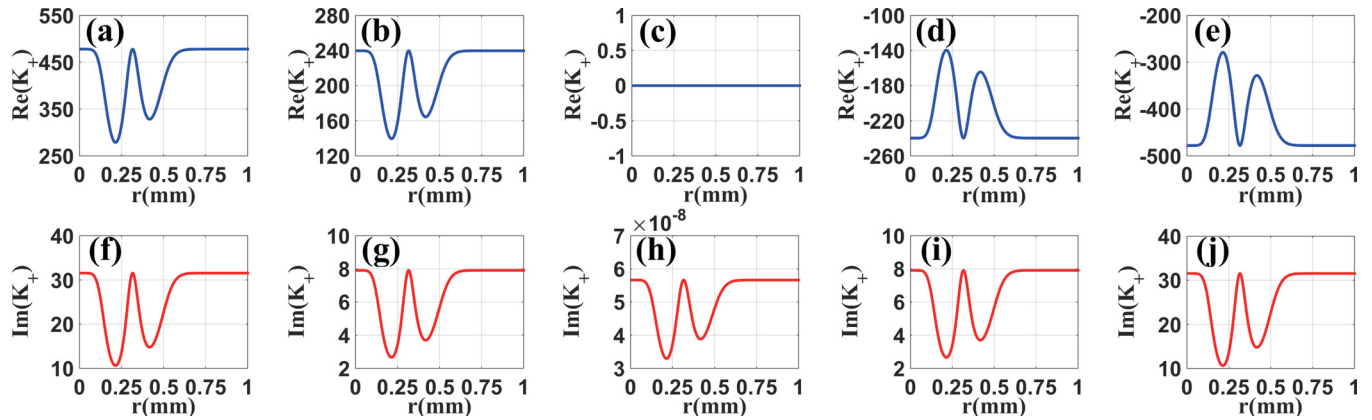


FIG. 3. The real [(a)–(e)] and imaginary [(f)–(j)] parts of the dispersion relation vs radius r for different detunings Δ_c : (a) and (f) $\Delta_c = -20$ meV, (b) and (g) $\Delta_c = -10$ meV, (c) and (h) $\Delta_c = 0$ meV, (d) and (i) $\Delta_c = 10$ meV, (e) and (j) $\Delta_c = 20$ meV. The other parameters are the same as in Fig. 2.

and outer ring ($r > \sqrt{2.5}\omega_0$) twist oppositely. Interestingly, when $\Delta_c = 10$ or 20 meV [see Figs. 2(d), 2(e), 2(i), and 2(j)], the intensity becomes weak but the rotated directions of the twisted phases within two rings are completely opposite compared with the cases in Figs. 2(a) and 2(b). Clearly, the phase and intensity of the FWM field is modulated via the detuning Δ_c .

In order to understand the above phenomena, we plot the real part and imaginary parts of the dispersion relation K_+ versus radius r for different detunings Δ_c in Fig. 3. For the case $\Delta_c = 0$, as shown Figs. 3(c) and 3(h), the imaginary part is very small ($\sim 10^{-8}$) and the real part is always equal to zero, so the phase is not twisted in Fig. 2(c). However, when $\Delta_c = \pm 10$ or ± 20 meV, both the real part and imaginary parts increase remarkably [see Figs. 3(a), 3(b), 3(d), 3(e), 3(f), and 3(g), 3(i), and 3(j)], which means that the spatial dependencies of the phase and absorption are increasing. So the phase is twisted in Figs. 2(a), 2(b), 2(d), and 2(e) while the value of intensity decreases in Figs. 2(f), 2(g), 2(i), and 2(j). Here, note that the value of the real part in Fig. 3(a) [or Fig. 3(b)] is positive compared with the negative value of the real part in Fig. 3(d) [or Fig. 3(e)], which gives the reasonable reason that the rotated directions of the twisted phase are opposite between Figs. 2(a) and 2(e) [or between Figs. 2(b) and 2(d)]. Moreover, the imaginary part in Fig. 3(f) [or Fig. 3(g)] is the same as in Fig. 3(j) [or Fig. 3(i)], which is in good agreement with the same intensity profiles in Figs. 2(f) and 2(j) [or in Figs. 2(g) and 2(i)].

In Fig. 4, we study the effect of the intensity of the control field Ω_c on the FWM field. From this figure, by increasing the control field, one can see that the FWM field is significantly enhanced and its phase twist is almost completely suppressed in Fig. 4(c). Actually, states $|1\rangle$, $|2\rangle$, and $|3\rangle$ construct a standard EIT system. By tuning the intensity of the control field Ω_c , the linear and nonlinear responses of the sample can be easily controlled, which result in the enhancement of FWM and the suppression of phase twist. Similarly, we display the real and imaginary parts of the dispersion relation versus radius r for different intensities of the control field Ω_c in Fig. 5. Obviously, with increasing the control field, both the

real part and imaginary parts are suppressed, which readily verifies the findings in Fig. 4.

We note that, very recently, a theoretical scheme for controlling the spatially dependent FWM in SQWs has been proposed [34]. In that scheme, an asymmetric semiconductor three-coupled-quantum-well system was used to manipulate the FWM via the detuning of a control field. Comparing with that scheme, the major differences in our proposal are the following. First, the main difference between our scheme and the one in Ref. [34] is that we have utilized the intensity of the control field Ω_c to control the FWM field. Second, with increasing the control field Ω_c , the FWM field is enhanced and phase twist is almost completely suppressed, which are quite different from the results obtained in Ref. [34]. Third, the definition of detuning Δ_c is also different from the one in Ref. [34], where the detuning Δ_c is a single-photon detuning while in our work the detuning Δ_c is a two-photon detuning. In the two-photon detuning more parameters (e.g., the frequencies of the fields ω_c and ω_p) can be manipulated and hence one can select suitable frequencies of the fields to explore the singularity characteristics of spatially dependent wave fronts in nonlinear processes.

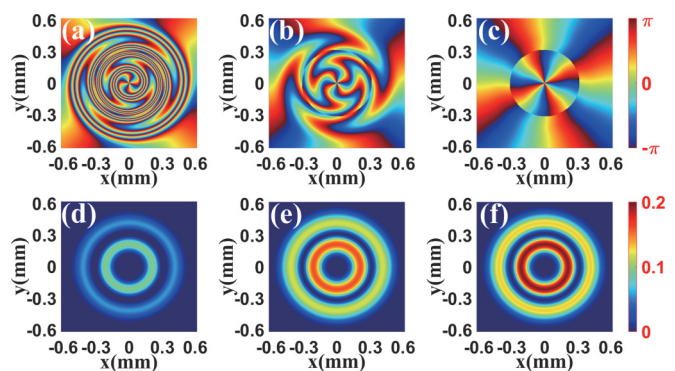


FIG. 4. (a)–(c) Phase patterns of the FWM field for different intensities of the control field Ω_c : (a) $\Omega_c = 15$ meV, (b) $\Omega_c = 25$ meV, (c) $\Omega_c = 35$ meV. (d)–(f) are the corresponding intensity patterns of the FWM field. Other parameters are the same as in Fig. 2(d).

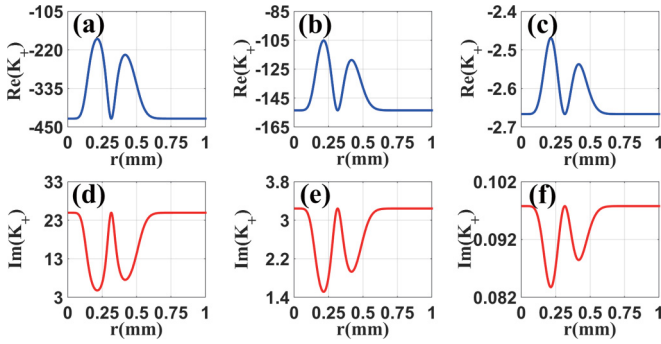


FIG. 5. The real $\text{Re}(K_+)$ and imaginary $\text{Im}(K_+)$ parts of the dispersion relation vs radius r for different intensities of the control field Ω_c : (a) and (d) $\Omega_c = 15$ meV, (b) and (e) $\Omega_c = 25$ meV, (c) and (f) $\Omega_c = 35$ meV. Other parameters are the same as in Fig. 2(d).

B. The superposition modes

For further studying the nonlinear process, next, we perform the superposition modes created by the interference between the FWM field and a same-frequency LG mode Ω^c , which is given as

$$\Omega^c = \begin{cases} \Omega_0^c \Omega(r) e^{i\phi l}, & 0 \leq r \leq \sqrt{0.5(|l|+1)}\omega_0, \\ \Omega_0^c \Omega(r) e^{-i\phi l}, & r \geq \sqrt{0.5(|l|+1)}\omega_0, \end{cases} \quad (10)$$

with $\Omega_0^c = 0.4$ meV. The superposition profiles are depicted in Figs. 6 and 7, respectively. Note that the superposition intensity (or phase) pattern appears as a result of the interference between the FWM field and the LG beam in a beam splitter.

In Fig. 6, we display the superposition mode created by the interference between the FWM field and the LG mode Ω^c for different detunings Δ_c . As shown in Figs. 6(c) and 6(h), when $\Delta_c = 0$, both the superposition phase and the superposition intensity are divided into eight parts within the inner ring ($0 \leq r \leq \sqrt{2.5}\omega_0$) and the outer ring ($r > \sqrt{2.5}\omega_0$). In the case of $\Delta_c = -10$ or -20 meV, the superposition phase profiles are twisted in the two rings [see Figs. 6(d) and 6(e)], while the superposition intensity is clockwise twisted in the outer

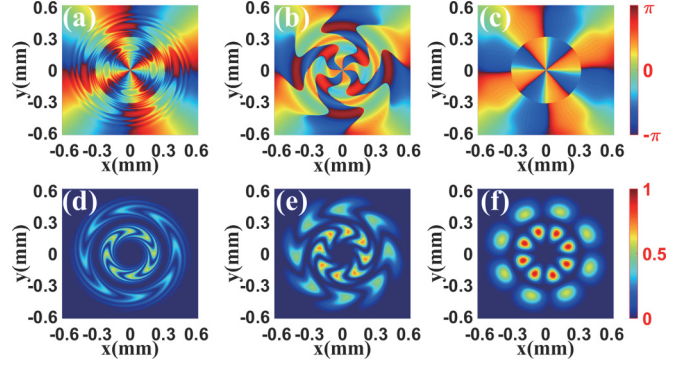


FIG. 7. The superposition phase [(a)–(c)] and intensity [(d)–(f)] profiles created by the interference between the FWM field and a same-frequency LG mode Ω^c for different intensities of the control field Ω_c : (a) and (d) $\Omega_c = 15$ meV, (b) and (e) $\Omega_c = 25$ meV, (c) and (f) $\Omega_c = 35$ meV. The other parameters are the same as in Fig. 2.

ring ($r > \sqrt{2.5}\omega_0$) but anticlockwise in the inner ring ($0 \leq r \leq \sqrt{2.5}\omega_0$) [see Figs. 6(i) and 6(j)]. Interestingly, when Δ_c is positive, the rotated directions of the twisted superposition phase within two rings are completely opposite compared with the cases where the values of Δ_c are positive [see Figs. 6(a) and 6(b)]. At the same time, the superposition intensity is clockwise twisted in the inner ring ($0 \leq r \leq \sqrt{2.5}\omega_0$) but twists anticlockwise in the outer ring ($r > \sqrt{2.5}\omega_0$). Obviously, the superposition mode is also modulated spatially.

In Fig. 7, we show another superposition mode created by the interference between the FWM field and the LG mode Ω^c for different intensities of the control field Ω_c . As we expected, different from Fig. 6, the twists of the superposition patterns are suppressed by increasing the intensity of the control field. The reason is that the intensity of the control field Ω_c modifies the azimuthal phase difference between the FWM field and the LG mode Ω^c , which results in the suppression of twisted superposition patterns. Actually, the results imply a more flexible intensity control for the superposition OAM modes via the intensity of the control field Ω_c .

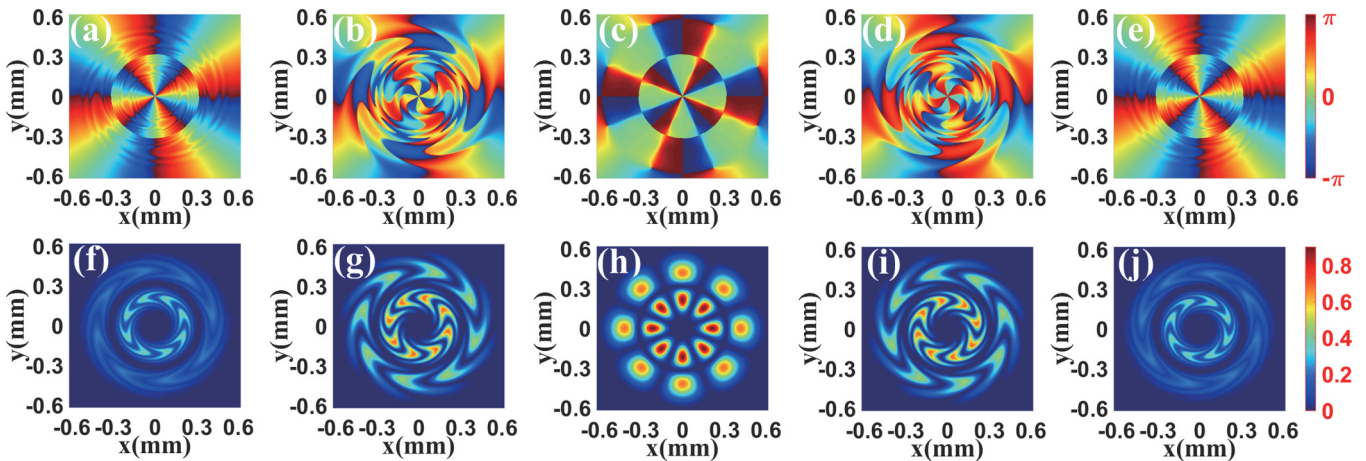


FIG. 6. The superposition phase [(a)–(e)] and intensity [(f)–(j)] profiles created by the interference between the FWM field and a same-frequency LG mode Ω^c for different detunings Δ_c : (a) and (f) $\Delta_c = -20$ meV, (b) and (g) $\Delta_c = -10$ meV, (c) and (h) $\Delta_c = 0$ meV, (d) and (i) $\Delta_c = 10$ meV, (e) and (j) $\Delta_c = 20$ meV. The other parameters are the same as in Fig. 2.

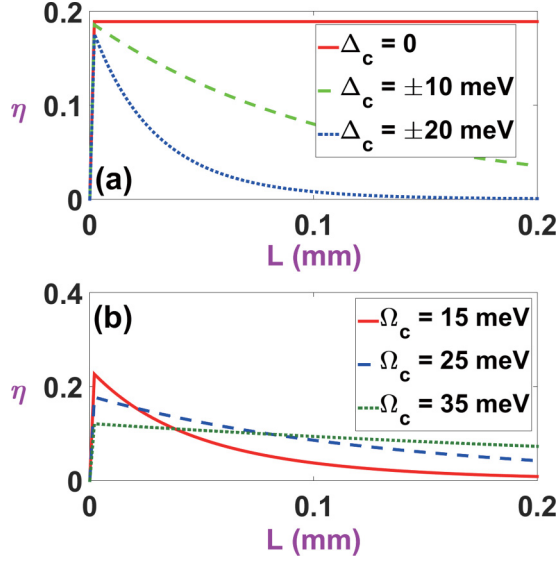


FIG. 8. The conversion efficiency η of the output FWM field vs propagation distance L for different (a) Δ_c and (b) Ω_c , respectively. Other parameters are the same as in Fig. 2.

C. Conversion efficiency for four-wave mixing

The conversion efficiency of the generated FWM field η after propagation distance L can be evaluated by comparing the electric energy of the output FWM field and the input probe field [57], such that $\eta = \iint |E_m(z=L, x, y)|^2 dx dy / \iint |E_p(z=0, x, y)|^2 dx dy$, where $E_m(z=L, x, y)$ is the electric energy of the generated FWM field at $z=L$ and $E_p(z=0, x, y)$ is the electric energy of the probe field at $z=0$. In terms of the Rabi frequencies, one has $|E_m(z=L, x, y)|^2 = 4\hbar^2 |\Omega_m(z=L, x, y)|^2 / |\mu_{41}|^2$ and $|E_p(z=0, x, y)|^2 = 4\hbar^2 |\Omega_p(z=0, x, y)|^2 / |\mu_{31}|^2$. Then the FWM efficiency of the output FWM field can be written as

$$\eta = \frac{|\mu_{31}|^2 \int_x \int_y |\Omega_m(z=L, x, y)|^2 dx dy}{|\mu_{41}|^2 \int_x \int_y |\Omega_p(z=0, x, y)|^2 dx dy}. \quad (11)$$

In order to study the FWM conversion efficiency, in Fig. 8 we plot the conversion efficiency η versus propagation distance L for different Δ_c and Ω_c , respectively. In Fig. 8(a), we present the conversion efficiency η versus propagation distance L for different Δ_c . In the case of $\Delta_c = 0$ [see the solid line in Fig. 8(a)], the maximum conversion efficiency is nearly 20%. However, when the detuning is increased to ± 10 meV, the FWM conversion efficiency decreases with increasing propagation distance [see the dashed line in Fig. 8(a)]. As we further increase the detuning, i.e., $\Delta_c = \pm 20$ meV, the conversion efficiency dramatically decreases with L [see the dotted line in Fig. 8(a)]. As shown in Fig. 8(b), we take into account the control field $\Omega_c = 15$ meV, and the maximum FWM efficiency is more than 20% [see the solid line in Fig. 8(b)]. When the control field Ω_c is tuned to 25 meV, the maximum FWM efficiency is decreasing [see the dashed-dotted line in Fig. 8(b)]. For the case $\Omega_c = 35$ meV, the maximum efficiency decreases remarkably [see the dotted line in Fig. 8(b)]. It is pointed out that the findings in Fig. 8 agree very well with the results in Figs. 2–7.

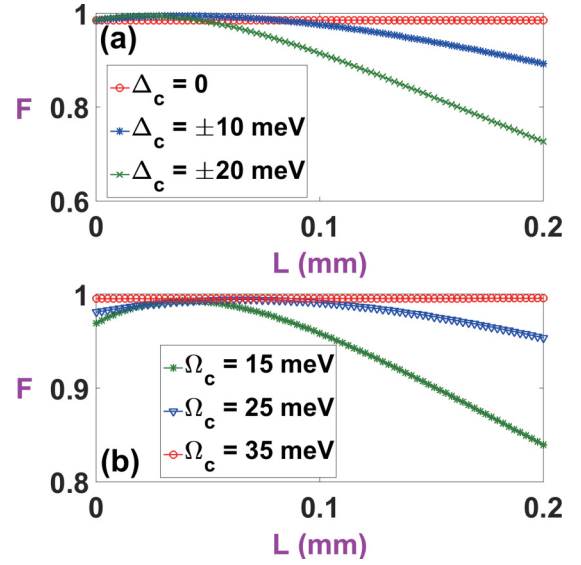


FIG. 9. The normalized fidelity F of the output FWM field vs propagation distance L for different (a) Δ_c and (b) Ω_c , respectively. Other parameters are the same as in Fig. 2.

D. Fidelity of four-wave mixing

Finally, to determine the quality of the output FWM field in comparison to the input OAM field, we define the normalized fidelity F based on Ref. [58], which quantifies how faithfully the output FWM field is generated ($0 \leq F \leq 1$, where 1 represents perfectly correlated complex fields). This can be calculated from the overlap integral of the output FWM field $\Omega_m(z=L, x, y)$, which actually transferred from the OAM field $\Omega_v(z=0, x, y)$,

$$F = \left| \frac{\int_x \int_y \Omega_m(z=L, x, y) \Omega_v^*(z=0, x, y) dx dy}{N_f} \right|^2, \quad (12)$$

where $N_f = (\int_x \int_y |\Omega_v(z=0, x, y)|^2 dx dy)^{1/2} \times (\int_x \int_y |\Omega_m(z=L, x, y)|^2 dx dy)^{1/2}$ is the normalization constant.

In Fig. 9, we display the normalized fidelity F of the output FWM field versus propagation distance L for different Δ_c and Ω_c , respectively. Figure 9(a) shows the effect of the detuning of the control field Δ_c on the normalized fidelity F . By increasing the detuning Δ_c , the maximum fidelity decreases dramatically when the propagation distance L increases. With increasing the intensity of the control field Ω_c , as shown in Fig. 9(b), the results are completely contrary to Fig. 9(a) and the normalized fidelity F increases. More interestingly, for the case where $\Omega_c = 35$ meV, the fidelity of the output FWM field is approximately 100% [see the line marked with \circ in Fig. 9(b)]; that is to say, the high-fidelity FWM mode is indeed achieved.

IV. CONCLUSIONS

In conclusion, we propose a scheme to study spatiotemporal-vortex four-wave mixing (FWM) in an asymmetric SDQW nanostructure. The FWM field,

transferred from a unique OAM mode, can be modulated via detuning or the intensity of the control field. The superposition modes created by the interference between the FWM field and a same-frequency LG mode are also studied, showing many interesting properties. More importantly, high conversion efficiency is achieved and the generated FWM mode can have a maximum fidelity of approximately 100%. Thus, our method and analysis could be useful in investigating

the OAM-based quantum phenomena in nanostructures [59–66].

ACKNOWLEDGMENTS

We thank Prof. B.-S. Shi (USTC) for valuable discussions. The work is supported by National Natural Science Foundation of China (Grant No. 11674002).

-
- [1] L. Allen, M. W. Beijersbergen, R. J. C. Spreeuw, and J. P. Woerdman, *Phys. Rev. A* **45**, 8185 (1992).
- [2] M. Padgett, J. Courtial, and L. Allen, *Phys. Today* **57**(5), 35 (2004).
- [3] J. W. R. Tabosa and D. V. Petrov, *Phys. Rev. Lett.* **83**, 4967 (1999).
- [4] S. Barreiro, J. W. R. Tabosa, J. P. Torres, Y. Deyanova, and L. Torner, *Opt. Lett.* **29**, 1515 (2004).
- [5] H. Wang, C. Fabre, and J. Jing, *Phys. Rev. A* **95**, 051802(R) (2017).
- [6] Z. Zhang, D. Ma, Y. Zhang, M. Cao, Z. Xu, and Y. Zhang, *Opt. Lett.* **42**, 1059 (2017).
- [7] S. Barreiro and J. W. R. Tabosa, *Phys. Rev. Lett.* **90**, 133001 (2003).
- [8] A. M. Marino, V. Boyer, R. C. Pooser, P. D. Lett, K. Lemons, and K. M. Jones, *Phys. Rev. Lett.* **101**, 093602 (2008).
- [9] G. Walker, A. S. Arnold, and S. Franke-Arnold, *Phys. Rev. Lett.* **108**, 243601 (2012).
- [10] H. R. Hamed, J. Ruseckas, and G. Juzeliūnas, *Phys. Rev. A* **98**, 013840 (2018).
- [11] H. R. Hamed, E. Paspalakis, G. Žlabys, G. Juzeliūnas, and J. Ruseckas, *Phys. Rev. A* **100**, 023811 (2019).
- [12] Y. Hong, Z. Wang, D. Ding, and B. Yu, *Opt. Express* **27**, 29863 (2019).
- [13] N. S. Mallick and T. N. Dey, *J. Opt. Soc. Am. B* **37**, 1857 (2020).
- [14] H. R. Hamed, J. Ruseckas, E. Paspalakis, and G. Juzeliūnas, *Phys. Rev. A* **101**, 063828 (2020).
- [15] R. Pugatch, M. Shuker, O. Firstenberg, A. Ron, and N. Davidson, *Phys. Rev. Lett.* **98**, 203601 (2007).
- [16] D. S. Ding, W. Zhang, Z. Y. Zhou, S. Shi, G. Y. Xiang, X. S. Wang, Y. K. Jiang, B. S. Shi, and G. C. Guo, *Phys. Rev. Lett.* **114**, 050502 (2015).
- [17] V. Parigi, V. Ambrosio, C. Arnold, L. Marrucci, F. Sciarrino, and J. Laurat, *Nat. Commun.* **6**, 7706 (2015).
- [18] X. Pan, S. Yu, Y. Zhou, K. Zhang, K. Zhang, S. Lv, S. Li, W. Wang, and J. Jing, *Phys. Rev. Lett.* **123**, 070506 (2019).
- [19] K. Zhang, W. Wang, S. Liu, X. Pan, J. Du, Y. Lou, S. Yu, S. Lv, N. Treps, C. Fabre, and J. Jing, *Phys. Rev. Lett.* **124**, 090501 (2020).
- [20] G. B. Serapiglia, E. Paspalakis, C. Sirtori, K. L. Vodopyanov, and C. C. Phillips, *Phys. Rev. Lett.* **84**, 1019 (2000).
- [21] M. C. Phillips and H. Wang, *Phys. Rev. Lett.* **89**, 186401 (2002).
- [22] M. C. Phillips and H. Wang, *Opt. Lett.* **28**, 831 (2003).
- [23] J. F. Dynes, M. D. Frogley, J. Rodger, and C. C. Phillips, *Phys. Rev. B* **72**, 085323 (2005).
- [24] J. H. Wu, J. Y. Gao, J. H. Xu, L. Silvestri, M. Artoni, G. C. La Rocca, and F. Bassani, *Phys. Rev. Lett.* **95**, 057401 (2005).
- [25] M. D. Frogley, J. F. Dynes, M. Beck, J. Faist, and C. C. Phillips, *Nat. Mater.* **5**, 175 (2006).
- [26] H. Sun, S. Gong, Y. Niu, S. Jin, R. Li, and Z. Xu, *Phys. Rev. B* **74**, 155314 (2006).
- [27] J. H. Li, *Phys. Rev. B* **75**, 155329 (2007).
- [28] W. X. Yang, J. M. Hou, and R. K. Lee, *Phys. Rev. A* **77**, 033838 (2008).
- [29] C. J. Zhu and G. X. Huang, *Phys. Rev. B* **80**, 235408 (2009).
- [30] X. Hao, J. Li, J. Liu, P. Song, and X. Yang, *Phys. Lett. A* **372**, 2509 (2008).
- [31] S. Evangelou and E. Paspalakis, *Photonics Nanostruct.: Fundam. Appl.* **9**, 168 (2011).
- [32] H. Sun, S. Fan, H. Zhang, and S. Gong, *Phys. Rev. B* **87**, 235310 (2013).
- [33] S. Liu, W. X. Yang, Y. L. Chuang, A. X. Chen, A. Liu, and Y. Huang, *Opt. Express* **22**, 29179 (2014).
- [34] Y. Zhang, Z. Wang, J. Qiu, Y. Hong, and B. Yu, *Appl. Phys. Lett.* **115**, 171905 (2019).
- [35] J. Qiu, Z. Wang, D. Ding, W. Li, and B. Yu, *Opt. Express* **28**, 2975 (2020).
- [36] Rahmatullah, M. Abbas, Ziauddin, and S. Qamar, *Phys. Rev. A* **101**, 023821 (2020).
- [37] M. Mahdavi, Z. Amini Sabegh, M. Mohammadi, M. Mahmoudi, and H. R. Hamed, *Phys. Rev. A* **101**, 063811 (2020).
- [38] Y. Zhang, A. W. Brown, and M. Xiao, *Phys. Rev. Lett.* **99**, 123603 (2007).
- [39] D. S. Ding, Z. Y. Zhou, B. S. Shi, X. B. Zhou, and G. C. Guo, *Opt. Lett.* **37**, 3270 (2012).
- [40] A. M. Akulshin, R. J. McLean, E. E. Mikhailov, and I. Novikova, *Opt. Lett.* **40**, 1109 (2015).
- [41] N. Prajapati, N. Super, N. R. Lanning, J. P. Dowling, and I. Novikova, *Opt. Lett.* **44**, 739 (2019).
- [42] J. Faist, F. Capasso, C. Sirtori, K. W. West, and L. N. Pfeiffer, *Nature (London)* **390**, 589 (1997).
- [43] J. F. Dynes and E. Paspalakis, *Phys. Rev. B* **73**, 233305 (2006).
- [44] E. Paspalakis, M. Tsaousidou, and A. F. Terzis, *Phys. Rev. B* **73**, 125344 (2006).
- [45] A. A. Zhdanova, M. Shutova, A. Bahari, M. Zhi, and A. V. Sokolov, *Opt. Express* **23**, 34109 (2015).
- [46] N. Radwell, T. W. Clark, B. Piccirillo, S. M. Barnett, and S. Franke-Arnold, *Phys. Rev. Lett.* **114**, 123603 (2015).
- [47] S. Sharma and T. N. Dey, *Phys. Rev. A* **96**, 033811 (2017).
- [48] X. Yang, Y. Chen, J. Wang, Z. Dou, M. Cao, D. Wei, H. Batelaan, H. Gao, and F. Li, *Opt. Lett.* **44**, 2911 (2019).
- [49] J. Faist, C. Sirtori, F. Capasso, L. Pfeiffer, and K. W. West, *Appl. Phys. Lett.* **64**, 872 (1994).

- [50] C. Sirtori, F. Capasso, D. L. Sivco, and A. Y. Cho, *Phys. Rev. Lett.* **68**, 1010 (1992).
- [51] A. M. Yao and M. J. Padgett, *Adv. Opt. Photonics* **3**, 161 (2011).
- [52] B. P. da Silva, V. A. Pinillos, D. S. Tasca, L. E. Oxman, and A. Z. Khoury, *Phys. Rev. Lett.* **124**, 033902 (2020).
- [53] W. T. Buono, A. Santos, M. R. Maia, L. J. Pereira, D. S. Tasca, K. Dechoum, T. Ruchon, and A. Z. Khoury, *Phys. Rev. A* **101**, 043821 (2020).
- [54] T. Shih, K. Reimann, M. Woerner, T. Elsaesser, I. Waldmüller, A. Knorr, R. Hey, and K. H. Ploog, *Phys. Rev. B* **72**, 195338 (2005).
- [55] Y. Wu and X. Yang, *Phys. Rev. A* **70**, 053818 (2004).
- [56] Y. Wu and X. Yang, *Phys. Rev. B* **76**, 054425 (2007).
- [57] Y. Wu, M. G. Payne, E. W. Hagley, and L. Deng, *Opt. Lett.* **29**, 2294 (2004).
- [58] R. Liu, F. Li, M. J. Padgett, and D. B. Phillips, *Optica* **2**, 1028 (2015).
- [59] S. M. Sadeghi, S. R. Leffler, and J. Meyer, *Phys. Rev. B* **59**, 15388 (1999).
- [60] S. M. Sadeghi, H. M. van Driel, and J. M. Fraser, *Phys. Rev. B* **62**, 15386 (2000).
- [61] S. M. Sadeghi, *Nanotechnology* **20**, 225401 (2009).
- [62] A. Hatef, S. M. Sadeghi, and M. R. Singh, *Nanotechnology* **23**, 065701 (2012).
- [63] F. Carreño and M. A. Antón, *Phys. Rev. B* **93**, 125301 (2016).
- [64] F. Carreño, M. A. Antón, V. Yannopoulos, and E. Paspalakis, *Phys. Rev. B* **95**, 195410 (2017).
- [65] S. M. Sadeghi, R. R. Gutha, and W. J. Wing, *J. Phys. Chem. C* **124**, 4261 (2020).
- [66] M. R. Singh and S. Yastrebov, *J. Phys. Chem. C* **124**, 12065 (2020).